

Theoretical Formulation of Collision Rate and Collision Efficiency of Hydrodynamically Interacting Cloud Droplets in Turbulent Atmosphere

LIAN-PING WANG, ORLANDO AYALA, AND SCOTT E. KASPRZAK

Department of Mechanical Engineering, University of Delaware, Newark, Delaware

WOJCIECH W. GRABOWSKI

Mesoscale and Microscale Meteorology Division, National Center for Atmospheric Research, Boulder, Colorado

(Manuscript received 3 May 2004, in final form 12 December 2004)

ABSTRACT

A methodology for conducting direct numerical simulations (DNSs) of hydrodynamically interacting droplets in the context of cloud microphysics has been developed and used to validate a new kinematic formulation capable of describing the collision rate and collision efficiency of cloud droplets in turbulent air. The theoretical formulation is formally the same as the formulation recently developed for geometrical collision rate of finite-inertia, nonsettling particles. It is shown that its application to hydrodynamically interacting droplets requires corrections because of a nonoverlap requirement. An approximate method for correcting the kinematic properties has been developed and validated against DNS data. The formulation presented here is more general and accurate than previously published formulations that, in most cases, are some extension to the description of hydrodynamic–gravitational collision. General dynamic and kinematic representations of the properly defined collision efficiency in a turbulent flow have been discussed. In addition to augmenting the geometric collision rate, air turbulence has been found to enhance the collision efficiency because, in a turbulent flow, hydrodynamic interactions become less effective in reducing the average relative radial velocity. The level of increase in the collision efficiency depends on the flow dissipation rate. For example, the collision efficiency between droplets of 20 and 25 μm in radii is increased by 59% and 10% by air turbulence at dissipation rates of 400 and 100 $\text{cm}^2 \text{s}^{-3}$, respectively. It is also shown that hydrodynamic interactions lead to higher droplet concentration fluctuations. The formulation presented here separates the effect of turbulence on collision efficiency from the previously observed effect of turbulence on the geometric collision rate.

1. Introduction

Although the importance of turbulence on rain formation was noted more than 60 yr ago (Arenberg 1939), progress has been very slow in identifying and understanding the nature and quantitative importance of turbulence effects. Adequate treatment of the turbulence effects on droplet growth represents a major gap in our understanding of cloud microphysical processes (Beard and Ochs 1993; Shaw 2003). This slow progress is due to the complexities associated with turbulence–droplet interactions and the long-time lack of

quantitative research tools. In the last 15 yr, the availability of advanced computational research tools, such as the direct numerical simulations (DNS) of turbulent particle-laden flows has enabled researchers mainly in the engineering community to advance physical understanding and theoretical treatment of particle–turbulence interactions (Squires and Eaton 1990; Wang and Maxey 1993) and particle–particle collision rates in a turbulent flow (Sundaram and Collins 1997; Wang et al. 2000; Zhou et al. 2001).

Air turbulence in atmospheric clouds has the potential to modify the collision–coalescence process in at least three general ways (Jonas 1996; Shaw 2003). First, the relative velocity between two colliding droplets is affected by the unsteady, three-dimensional air velocity field and is usually larger than the differential terminal velocity in still air (Saffman and Turner 1956; Wang et

Corresponding author address: Dr. Lian-Ping Wang, Dept. of Mechanical Engineering, University of Delaware, 126 Spencer Laboratory, Newark, DE 19716-3140.
E-mail: lwang@me.udel.edu

al. 1998b; Dodin and Elperin 2002; Franklin et al. 2005).¹ Second, in local regions of the flow where the air streamlines are severely curved (e.g., regions of high vorticity or high strain rate), droplets, as a result of their finite inertia, can be nonuniformly distributed (Maxey 1987; Squires and Eaton 1990; Wang and Maxey 1993), leading to potentially much higher rates of collisions on average (Sundaram and Collins 1997; Wang et al. 2000; Zhou et al. 2001). Third, turbulence may also alter the local droplet–droplet hydrodynamic interactions and collision efficiencies as both the magnitude and orientation of droplet–droplet relative motion and local droplet distribution can be altered by local turbulent characteristics over a range of length and time scales much wider than the time and length scales represented by the droplets (de Almeida 1976, 1979; Grover and Pruppacher 1985; Koziol and Leighton 1996; Pinsky et al. 1999; Franklin et al. 2005).

In this paper, we focus on the effect of air turbulence on collision efficiency, a topic that perhaps is least understood in collision–coalescence microphysics. For the hydrodynamic–gravitational problem without air turbulence, the collision efficiency is often defined simply as (Pruppacher and Klett 1997)

$$E_{12}^g = \frac{y_c^2}{R^2}, \quad (1)$$

where y_c is the far-field, off-center horizontal separation of the grazing trajectory of the smaller droplet relative to the larger droplet, the geometric collision radius R is the sum of the radii of two colliding droplets, $R = a_1 + a_2$. If both droplets are small and the disturbance flows can be modeled as a quasi-steady Stokes flow, the collision efficiencies can be determined theoretically, for example, see Davis and Sartor (1967). For the more general, droplet–droplet hydrodynamic–gravitational problem at small but finite droplet Reynolds numbers, only approximate theoretical treatments are possible. The study of Klett and Davis (1973) provides typical results of collision efficiencies at small droplet Reynolds numbers using a superposition of Oseen disturbance flow solutions.

The undisturbed, or background, air turbulence complicates the determination of collision efficiencies in at least two aspects. First, the relative motion of any two droplets, before they can feel the disturbance flow field

caused by the other droplet, is far more complicated than the hydrodynamic–gravitational problem. Second, the disturbance flows induced by the droplets and their effects on the near-field droplet–droplet relative motion, namely, droplet–droplet hydrodynamic interactions, will also be modified by the small-scale features (i.e., local straining and rotational fluid motion) of the background air turbulence. Furthermore, the hydrodynamic interaction radius is typically 20 to 50 times the droplet radius and as such may exceed the Kolmogorov length of the turbulence when the flow dissipation rate is sufficiently large.

As we shall demonstrate in this paper, these complications make the concept of relative grazing trajectory not so useful for hydrodynamic interactions in a turbulent flow. Specifically, for the case of nearly equal-size droplets, the relative motion due to turbulence can be larger than that due to differential terminal velocity; therefore, the smaller droplet could approach and collide with the larger droplet from almost any direction relative to the larger droplet. In such a case, the quantity y_c in Eq. (1) can no longer be properly defined.

The main objective of this paper is to introduce and develop a general, kinematic formulation that can describe the collision kernel of hydrodynamically interacting droplets in turbulent air. Such a formulation has been developed and validated for geometrical collision rates of nonsettling particles in turbulent flow without hydrodynamic interactions (Sundaram and Collins 1997; Wang et al. 1998b, 2000). We will show that the same formulation will apply to the case with hydrodynamic interactions and gravitational settling provided that corrections are made to the kinematic properties due to a nonoverlapping requirement. Direct numerical simulations combining pseudospectral simulations of air turbulence and approximate analytical representation of local disturbance flows are used to validate the corrections.

It is important to note that only a very few studies exist in the literature regarding collision efficiencies of cloud droplets in turbulent air. Table 1 summarizes these previous studies. One immediately notices that different kinematic formulations were used to define the collision efficiency, almost all of which are some extensions to Eq. (1). These definitions of collision efficiency were used in their studies without direct validation using dynamic collision statistics. This problem along with different, inaccurate representations of the air turbulence and different droplet-size combinations has generated somewhat controversial conclusions regarding the influence of turbulence on collision efficiencies.

The second objective of this paper is to introduce a

¹ The terms particles and droplets are used interchangeably in this paper. Cloud droplets are small and behave like solid particles as far as the viscous drag is concerned (Pruppacher and Klett 1997). Particles is a more general term for other applications for which the current study may also be applied.

TABLE 1. Collision efficiencies in turbulent flow: previous formulations and results.

	de Almeida (1976, 1979)	Grover and Pruppacher (1985)	Kozoil and Leighton (1996)	Pinsky et al. (1999)
E_{12}	$\frac{2}{R^2} \int_0^\infty yP(y) dy$	$\langle \Gamma_{12} \rangle / (\pi R^2 v_d)$	$\frac{R_0^2}{R^2} \int_0^\pi P(\theta; R_0) \sin(2\theta) d\theta$	$\langle S_c \rangle / (\pi R^2)$
(a_1, a_2) (μm)	(25, 10 \rightarrow 20)	(40 \rightarrow 100, 1 \rightarrow 5)	(10 \rightarrow 20, 2 \rightarrow 19)	(10 \rightarrow 30, 1 \rightarrow 29)
ϵ ($\text{cm}^2 \text{s}^{-3}$)	10	100	100	100
E_{12}/E_{12}^*	3.40 \rightarrow 5.49	Up to 100	≤ 1.60	2.0 \rightarrow 4.0
HI model	Klett and Davis (1973)	Numerical flow	Stokes flow	Stokes flow
Turbulence	2D eddy flow	1D eddy flow	3D random field	3D random field

more general definition of collision efficiency that is consistent with a definition based on statistics of dynamic collision events. Our formulation will separate the effect of turbulence on collision efficiency from the previously observed effect of turbulence on geometric collision rate, and is applicable for nonsettling particles as well.

The paper is organized as follows. In section 2, an overview of recent advances on the formulation of geometric collision rates in turbulent flow is presented, followed by the extension to the case with hydrodynamic interactions. Corrections due to a nonoverlapping requirement are developed. In section 3, a brief description of direct numerical simulations is given. Results from DNS are presented and compared with the theoretical formulation in section 4 mainly for the purpose of validating and understanding the theoretical formulation. Finally, conclusions are provided in section 5.

2. Theoretical considerations

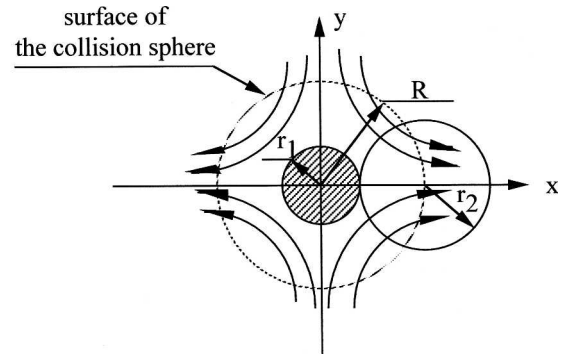
Most publications in the atmospheric sciences community utilize kinematic formulations of collision rates that are not too much different from those used for gravitational coagulation. In these formulations, the swept volume of a droplet was defined based on the concept of a collision cylinder as shown in Fig. 1b. As pointed out in Wang et al. (1998b), the formulation suggested by Saffman and Turner (1956), on the other hand, was based on the concept of a collision sphere (Fig. 1a). Wang et al. (1998b) showed that the spherical formulation is more general than the cylindrical formulation in the sense that the spherical formulation will recover the results for situations when the cylindrical formulation is correct (e.g., the gravitational coagulation). For the case of particle coagulation in a turbulent flow, the spherical formulation produces correct results, while the commonly used cylindrical formulation overpredicts the collision kernel (Wang et al. 1998b). We shall first review the spherical formulation and its recent developments.

a. Theoretical formulation of geometric collision kernel

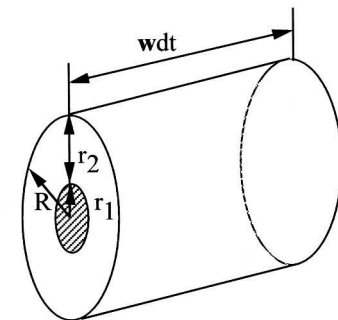
In general, the average collision kernel Γ_{12} is an average rate coefficient defined as

$$\Gamma_{12}^D = \frac{\langle \mathcal{N}_{12} \rangle}{n_1 n_2}, \tag{2}$$

where $\langle \mathcal{N}_{12} \rangle$ is the average number of collisions per unit time per unit volume between two size groups of average number concentrations n_1 and n_2 . In DNS, all col-



(a) Projection of the collision sphere on the x-y plane



(b) The concept of the collision cylinder

FIG. 1. Geometrical description of spherical and cylindrical formulations.

lision events can be detected and so $\langle \dot{\mathcal{N}}_{12} \rangle$ can be directly obtained. We shall refer to the collision kernel computed by Eq. (2) as the dynamic collision kernel (hence the superscript D).

When hydrodynamic interactions are not considered, Saffman and Turner (1956) proposed that the average geometrical collision kernel between two arbitrary particle size groups can be described kinematically as the average volume of fresh fluid entering a collision sphere per unit time,

$$\Gamma_{12}^K = 2\pi R^2 \langle |w_r|(r=R) \rangle. \quad (3)$$

The collision sphere is defined, relative to a reference particle, as a sphere of radius equal to the geometric collision radius $R = a_1 + a_2$, centered on the reference particle (Fig. 1a). Here, w_r is the radial component of the relative velocity \mathbf{w} between two particles, namely, $w_r = \mathbf{w} \cdot \mathbf{r}/r$, \mathbf{r} is the relative separation vector, and $r = |\mathbf{r}|$. One important assumption of Eq. (3) is that the relative velocity \mathbf{w} is incompressible, thus influx and outflux over the sphere surface are equal. The collision kernel is then half the surface area multiplied by the average magnitude of the radial relative velocity. Furthermore, the local particle concentrations are assumed to be uniform, making the formulation only applicable to zero relative-inertia particles having no preferential concentrations. The above formulation was validated by Wang et al. (1998a) using DNS, namely, they showed that for zero-inertia particles

$$\Gamma_{12}^K = \Gamma_{12}^D. \quad (4)$$

As shown by Wang et al. (1998b), Eq. (3) recovers the well-known gravitational collision kernel

$$\Gamma_{12}^g = \pi R^2 |W_1 - W_2|, \quad (5)$$

since for the pure gravitation case, $\langle |w_r|(r=R) \rangle = 0.5|W_1 - W_2|$. Here W_1 and W_2 are the terminal velocities of the droplets.

When particles have finite relative inertia, namely, the inertial response time of the particle $\tau_p = 2\rho_p a^2/(9\mu)$ is comparable to the Kolmogorov time scale, τ_k , of the air turbulence, particles are known to accumulate in regions of high strain and low vorticity (Maxey 1987). This preferential concentration effect can significantly increase the average collision kernel since the local collision rate is proportional to the second-order moment of local concentrations. Here, ρ_p is the density of the particle, a is the radius of the particle, μ is the fluid dynamic viscosity. The first theoretical formulation of

Γ_{12}^K for finite-inertia particles was developed by Sundaram and Collins (1997), which, after a correction made by Wang et al. (1998b, 2000), states

$$\Gamma_{12}^K = 2\pi R^2 \langle |w_r(r=R)| \rangle g_{12}(r=R), \quad (6)$$

where $g_{12}(r)$ is the radial distribution function and measure the effect of preferential concentration on the pair number density at separation r . In direct numerical simulations, g_{12} can be computed as, at any given time,

$$g_{12}(r; t) = \frac{N_{\text{pair}}/V_s}{N_1 N_2 / V_B}, \quad (7)$$

where N_{pair} is the total number of pairs detected with separation distance falling in a spherical shell of inner radius equal to $r_1 \equiv r - \delta_1$ and outer radius equal to $r_2 \equiv r + \delta_2$. Here, δ_1 and δ_2 are small fractions of r ; $V_s = 4\pi[(r + \delta_2)^3 - (r - \delta_1)^3]/3$ is the volume of the spherical shell; N_1 is the total number of size-1 particles used in the simulation, and N_2 is the total number of size-2 particles; V_B is the volume of the computational domain. Therefore,

$$n_1 = \frac{N_1}{V_B}, \quad n_2 = \frac{N_2}{V_B}. \quad (8)$$

The instantaneous radial distribution function $g_{12}(r; t)$ is further averaged over time to obtain $g_{12}(r)$. Similarly, $\langle |w_r(r)| \rangle$ is computed based on the particle pairs in the same spherical shell, by averaging the pair-relative velocities over all pairs detected and over time.

Physical interpretations of the geometric kinematical terms in Eq. (6) are the following: $2\pi R^2$ is half the surface area of the geometric collision sphere, $\langle |w_r(r=R)| \rangle$ is the average magnitude of relative flux per unit area per unit pair number density at the surface of the geometric collision sphere, and $g_{12}(r=R)$ is an enhancement factor due to locally nonuniform particle concentration fields.

The kinematic formulation, given by (6), has been validated in direct numerical simulations for a monodisperse system of nonsettling particles by Wang et al. (2000) and for a bidisperse system of nonsettling particles by Zhou et al. (2001), provided that the particle concentration fields are statistically stationary so that the net radial relative inward flux is the same as the net radial relative outward flux.

In summary, there are two alternative methods to obtain the collision kernel in direct numerical simulations. The first is based on Eq. (2) by dynamic detection of all collision events. The second is based on Eq. (6) by computing the kinematic properties relevant to collision dynamics.

b. Corrections to kinematics because of nonoverlap

When hydrodynamic interactions are not considered, each particle moves as if other particles were not present. Therefore, in previous simulations, we allowed particles to overlap in space and stay in the flow even when they participate in collision events (the so-called ghost particles). This was done mainly to keep the system truly stationary. Obviously, we could have chosen different postcollision treatments such as removing all particles from the system upon collisions so no overlap of particles in space is allowed. In a turbulent flow, it has been shown that different postcollision treatments of particles can lead to different collision rates (Zhou et al. 1998), as well as finite changes of kinematic properties near $r = R$. For example, Reade and Collins (2000) demonstrated that the distribution near $r = R$ of $g_{12}(r)$ for ghost particles could be quite different from that of finite-size, nonoverlap hard-sphere particles.

When hydrodynamic interactions are taken into account, particles can no longer overlap in space as this becomes unphysical. This also implies that droplets cannot penetrate through each other. In the DNS described later in this paper, a nonoverlap requirement is incorporated. Namely, every time a collision event occurs, we remove the pair from their current locations and, at the same time, add another two droplets having the same material properties as the pair just removed, back to the computational domain. The locations of the two added droplets are randomly chosen, and care is taken to make sure that they are not overlap with any other droplets in the system. Their velocities are set to their terminal velocity plus the local fluid velocity. They are then tracked by solving their equation of motion just like all other droplets. In this manner, the total number of particles remain the same and no particle overlaps with any other particles at the beginning of a time step. The above treatment mimics most closely the real situation of stochastic collision coalescence of cloud droplets, since coalescence of two droplets will remove these droplets from their own size groups while coalescence of smaller droplets can introduce new droplets to these size groups.

To understand how the nonoverlap requirement might affect the kinematic properties $\langle |w_r(r)| \rangle$ and $g_{12}(r)$, let us first consider the case of gravitational collisions without hydrodynamic interactions. Take a particle from the first size group as a reference particle, the relative motion of particles in the second size group is illustrated in Fig. 2. In this case, the distribution of the second-size particles is uniform everywhere except in the shaded region relative to a first-size particle where no second-size particles are found because of the non-

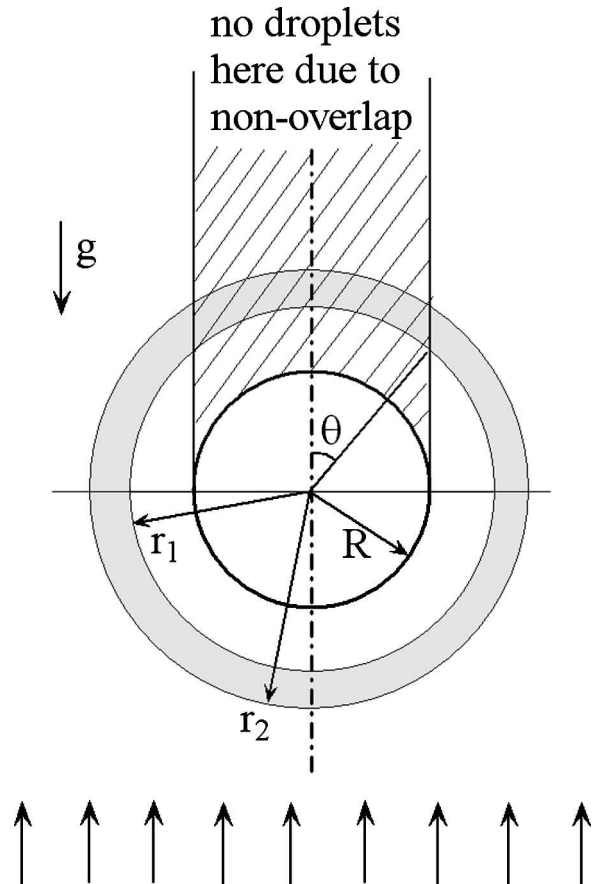


FIG. 2. The nonoverlapping and nonpenetration effects. The relative motion and distribution of the smaller-size droplets relative to a larger-size droplet.

overlap requirement. Therefore, the nonoverlap condition alters the symmetry of the problem for local spatial distribution of droplets.

The question is what will be the value of kinematic properties for this case. For this simple case, we can obtain their value theoretically. For a spherical shell at r of infinitesimal thickness, the right-hand side of Eq. (7) reduces to the percentage of surface area of the spherical surface at r that is outside the shaded region, namely,

$$g_{12}(r) = \frac{4\pi r^2 - \int_0^\theta (2\pi r \sin\theta')(r \, d\theta')}{4\pi r^2} = 0.5[1 + \sqrt{1 - (R/r)^2}], \quad (9)$$

where θ is the angle marking the edge of the shaded region and is given by $r \sin \theta = R$, as shown in Fig. 2. Similarly, the radial relative velocity can be obtained as follows:

$$\begin{aligned} \langle |w_r(r)| \rangle &= \left[\int_0^{\pi/2} (\Delta W \cos\theta') (2\pi r^2 \sin\theta' d\theta') \right. \\ &\quad \left. + \int_{\theta}^{\pi/2} (\Delta W \cos\theta') (2\pi r^2 \sin\theta' d\theta') \right] / 4\pi r^2 g_{12}(r) \\ &= \frac{\Delta W}{2} \frac{2 - R^2/r^2}{1 + \sqrt{1 - (R/r)^2}}. \end{aligned} \quad (10)$$

Next, consider a spherical shell of finite thickness with inner radius r_1 and outer radius r_2 on which actual computations of g_{12} and $\langle |w_r| \rangle$ are made in DNS. We have

$$\begin{aligned} g_{12}(r_1, r_2) &= \frac{\int_{r_1}^{r_2} 4\pi r^2 g_{12}(r) dr}{\int_{r_1}^{r_2} 4\pi r^2 dr} \\ &= 0.5 + 0.5[(r_2^2 - R^2)^{3/2} \\ &\quad - (r_1^2 - R^2)^{3/2}] / (r_2^3 - r_1^3), \end{aligned} \quad (11)$$

and

$$\begin{aligned} \langle |w_r(r_1, r_2)| \rangle &= \frac{\int_{r_1}^{r_2} \langle |w_r(r)| \rangle 4\pi r^2 g_{12}(r) dr}{\int_{r_1}^{r_2} 4\pi r^2 g_{12}(r) dr} \\ &= \frac{\Delta W}{2} \times \frac{1 - 1.5R^2(r_2 - r_1)/(r_2^3 - r_1^3)}{g_{12}(r_1, r_2)}. \end{aligned} \quad (12)$$

In DNS, we have used either 5% R or 1% R as the shell thickness to compute the values of g_{12} and $\langle |w_r| \rangle$ at contact. When the shell thickness is set at 1% R , Eqs. (11) and (12) yield the following:

$$\begin{aligned} g_{12}(R, 1.01R) &= 0.5470, \\ \langle |w_r(R, 1.01R)| \rangle &= 0.9232 \frac{\Delta W}{2}. \end{aligned} \quad (13)$$

Since the dynamic collision kernel remains the same, we conclude that the nonoverlap requirement reduces g_{12} by almost a half and w_r slightly. If the shell thickness is set at 5% R , we have

$$\begin{aligned} g_{12}(R, 1.05R) &= 0.6041, \\ \langle |w_r(R, 1.05R)| \rangle &= 0.8677 \frac{\Delta W}{2}. \end{aligned} \quad (14)$$

To recover the correct kinematic properties, we must remove these reductions. For this purpose, we propose the following rescaling rules to define the correct kinematic properties:

$$g_{12}(r) \equiv g_{12}^{\text{NO}} / g_{12}(r_1, r_2), \quad (15)$$

$$\langle |w_r|(r) \rangle \equiv \langle |w_r| \rangle^{\text{NO}} \times \frac{g_{12}(r_1, r_2)}{1 - 1.5R^2(r_2 - r_1)/(r_2^3 - r_1^3)}, \quad (16)$$

where $r = (r_1 + r_2)/2$, the superscript NO denotes values computed from DNS under the nonoverlap condition. The function $g_{12}(r_1, r_2)$ is defined by Eq. (11). The correction or rescaling factors depend on the shell thickness. It is assumed that the results obtained by Eqs. (15) and (16) are relatively insensitive to the exact thickness, $r_2 - r_1$, used if the thickness is made small. Obviously, the above corrections will ensure that the kinematic formulation, Eq. (6), remains valid for gravitational coagulation even when the nonoverlap condition is introduced.

Furthermore, we assume that the same correction rules can be applied to other coagulation mechanisms. In general, one should not expect that these rules, which are derived based on gravitational coagulation alone, can fully correct the kinematics. However, since all coagulation mechanisms share the same property that the net inward flux and net outward flux are balanced, and since the nonoverlap condition essentially takes away the outward flux near the surface of geometric collision sphere, we expect that the corrections to kinematic properties of droplet–droplet pairs at near-contact condition are similar for all coagulation mechanisms. This will be demonstrated by results from DNS in section 4.

c. Definition of collision efficiency in turbulent flow

A general collision efficiency in a turbulent flow can be defined as the ratio of the collision kernel with hydrodynamic interactions (HI) to the geometric collision kernel for droplets of the same size combination in the same turbulent flow or the reference collision kernel when the hydrodynamic interactions are not activated (No HI):

$$E_{12}^{\text{D}} = \frac{\Gamma_{12}^{\text{D}}(\text{HI})}{\Gamma_{12}^{\text{D}}(\text{No HI})}. \quad (17)$$

Alternatively, if the kinematic formulation applies to both cases with and without hydrodynamic interactions, we would have

$$E_{12}^{\text{K}} = \frac{\Gamma_{12}^{\text{K}}(\text{HI})}{\Gamma_{12}^{\text{K}}(\text{No HI})} = \frac{\langle |w_r| \rangle(\text{HI})}{\langle |w_r| \rangle(\text{No HI})} \times \frac{g_{12}(\text{HI})}{g_{12}(\text{No HI})}, \quad (18)$$

where it is implied that the kinematic properties are evaluated at $r = R$. This second method indicates that if the effects of hydrodynamic interactions on the rela-

tive velocity and pair distribution density could be quantified either theoretically or numerically, a parameterization method can be developed for the collision efficiency.

In the atmospheric sciences community, the collision kernel is often written relative to the reference case of hydrodynamic–gravitational coagulation (e.g., Prupacher and Klett 1997). As long as the collisions of droplets of unequal sizes are considered, we can write

$$\Gamma_{12} = \eta_G \eta_E \Gamma_{12}^g(\text{No HI}) E_{12}^g, \quad (19)$$

where $\Gamma_{12}^g(\text{No HI})$ is the geometrical gravitational collision kernel given by Eq. (5), E_{12}^g is the collision efficiency for the hydrodynamic–gravitational problem given by Eq. (1) and η_G represents an enhancement factor due to turbulence on the geometric collision kernel and is defined as

$$\eta_G = \frac{\Gamma_{12}(\text{No HI})}{\Gamma_{12}^g(\text{No HI})}. \quad (20)$$

Here, η_E represents an enhancement factor due to turbulence on the true collision efficiency and is defined as

$$\eta_E = \frac{E_{12}}{E_{12}^g}. \quad (21)$$

In the literature, the collision efficiency in a turbulent flow was not defined properly (e.g., see Table 1), often leading to the combination of the two enhancement factors, ($\eta_G \eta_E$), being incorrectly interpreted as the effect of turbulence on collision efficiency. For the hydrodynamic–gravitational problem, both enhancement factors reduce to 1, so our formulation is consistent with the established formulation for this simple situation.

3. Direct numerical simulations

Direct numerical simulations represent a unique and powerful research tool for quantitative investigation of turbulent collisions. In the recent past, they have provided a means to understand the essential physical mechanisms for turbulent collision processes and a database to examine new and old theoretical models, for example Sundaram and Collins (1997), Wang et al. (2000), and Zhou et al. (2001). In the context of turbulent collision of hydrodynamically interacting cloud droplets, there are five components to the development of DNS codes: (a) direct numerical simulation of background turbulent airflow, (b) a representation of disturbance flows due to the presence of droplets, (c) tracking the motion of cloud droplets, (d) dynamic detection of collision events, and (e) computation of relative velocity and radial distribution function. Most of

these, except (b), have been described in detail previously (Wang and Maxey 1993; Wang et al. 2000; Zhou et al. 2001) so only essential information will be provided below. A detailed description of (b) including validation procedures, code implementation issues, and optimization methods, is beyond the scope of this paper and is left for a separate paper.

a. Background air turbulence

We focus our attention on cloud droplets in the size range of 10 to 100 μm in radius for which the turbulent effects and gravitational collection are the primary relevant mechanisms for their interactions and growth. Since the droplet terminal velocity is on the order of flow Kolmogorov velocity and the Stokes response time is typically less than the Kolmogorov time (Grabowski and Vaillancourt 1999), turbulence–droplet interactions take place mainly in the viscous subrange. Therefore, the flow viscous dissipation rate ϵ is the key parameter in determining the droplet collision statistics.

The airflow in the core region of adiabatic cumulus clouds may be modeled as a homogeneous and isotropic turbulence (Vaillancourt and Yau 2000) by direct numerical simulations using a pseudospectral method. The incompressible, time-dependent, and three-dimensional Navier–Stokes equations,

$$\frac{\partial \mathbf{U}}{\partial t} = \mathbf{U} \times \boldsymbol{\omega} - \nabla \left(\frac{P}{\rho} + \frac{1}{2} \mathbf{U}^2 \right) + \nu \nabla^2 \mathbf{U} + \mathbf{f}(\mathbf{x}, t), \quad (22)$$

are solved along with the continuity equation $\nabla \cdot \mathbf{U} = 0$. Here, $\boldsymbol{\omega} \equiv \nabla \times \mathbf{U}$ is the flow vorticity, P is the pressure. The flow is generated from rest by the random forcing term $\mathbf{f}(\mathbf{x}, t)$, which is nonzero only for a few modes at low wave numbers. The flow becomes statistically stationary when, on average, the rate of viscous dissipation balances the rate of energy addition by the forcing term.

The small-scale features of the flow are characterized by the Kolmogorov scales that are defined based on the viscous dissipation rate ϵ and kinematic viscosity ν ; namely, the Kolmogorov length, time, velocity scale are

$$\eta = (\nu^3/\epsilon)^{1/4}; \quad \tau_k = (\nu/\epsilon)^{1/2}; \quad v_k = (\nu\epsilon)^{1/4}. \quad (23)$$

The large-scale features may be characterized by the rms fluctuation velocity u' or flow Taylor–microscale Reynolds number R_λ

$$u' \equiv \sqrt{\frac{\langle \mathbf{U} \cdot \mathbf{U} \rangle}{3}}, \quad R_\lambda = \sqrt{15} \left(\frac{u'}{v_k} \right)^2. \quad (24)$$

In DNS, the flow Taylor–microscale Reynolds number is typically two to three orders of magnitude smaller than in real clouds, so the effects of large-scale flow

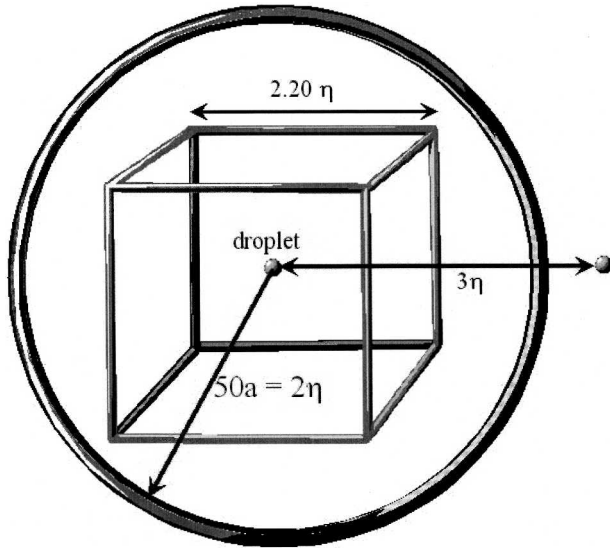


FIG. 3. Relative length scales in DNS. The cube represents the grid cell size in DNS, and the circle indicates the domain of influence for hydrodynamic interactions. For 64^3 DNS at $R_\lambda = 40$, the computational domain is about 141η , grid cell size is about 2.2η , and droplet diameter is 0.083η .

features could not be directly represented in DNS. The size of the computational domain is typically on the order of 10 cm or roughly 150η when a 64^3 DNS grid and a $400 \text{ cm}^2 \text{ s}^{-3}$ dissipation rate are used.

Since, in typical clouds, the droplet mass loading is on the order of 10^{-3} and volume fraction on the order of 10^{-6} , it is assumed that the presence of droplets has little effect on the background air turbulence.

b. Disturbance flows and hydrodynamic interactions

The disturbance flows due to droplets must be described for the purpose of incorporating droplet–droplet hydrodynamic interactions. The size of the computational grid cell in DNS is typically about 2η , which is one to two orders of magnitude larger than the radii of the droplets. Figure 3 illustrates the relative length scales in DNS. Obviously, the disturbance flows due to the droplets could not be resolved by the computational grid used for air turbulence simulation.

What we have used is a hybrid approach in which the disturbance flows are represented analytically. It is assumed that the droplets are much smaller than the flow Kolmogorov scale and the disturbance flows are spatially localized because of the strong viscous effect on the scale of droplet. Under this assumption, the disturbance flow around a droplet can be modeled as a quasi-steady Stokes flow. An improved superposition method has recently been developed (Wang et al. 2005), in

which the boundary conditions on the surface of each droplet is roughly satisfied. As a result, a more accurate representation of the force acting on a droplet because of the disturbance flows by all other droplets was developed. Wang et al. (2005) discussed the improved superposition method in detail when applied to two-droplet hydrodynamic interactions. Here we extend that formulation to a system containing arbitrary number of droplets.

Consider a suspension of N_p droplets in a turbulent flow of background velocity field $\mathbf{U}(\mathbf{x}, t)$. The composite air velocity field, after adding all the disturbance flow fields, is

$$\tilde{\mathbf{U}}(\mathbf{x}, t) \equiv \mathbf{U}(\mathbf{x}, t) + \sum_{k=1}^{N_p} \mathbf{u}_s[\mathbf{r}^{(k)}; a^{(k)}, \mathbf{V}^{(k)}] - \mathbf{U}(\mathbf{Y}^{(k)}, t) - \mathbf{u}^{(k)}, \quad (25)$$

where

$$\mathbf{u}_s(\mathbf{r}^{(k)}; a^{(k)}, \mathbf{V}^{(k)}) \equiv \left[\frac{3a^{(k)}}{4r^{(k)}} - \frac{3}{4} \left(\frac{a^{(k)}}{r^{(k)}} \right)^3 \right] \frac{\mathbf{r}^{(k)}}{(r^{(k)})^2} (\mathbf{V}^{(k)} \cdot \mathbf{r}^{(k)}) + \left[\frac{3a^{(k)}}{4r^{(k)}} + \frac{1}{4} \left(\frac{a^{(k)}}{r^{(k)}} \right)^3 \right] \mathbf{V}^{(k)}, \quad (26)$$

represents Stokes disturbance flow due to the k th droplet of radius $a^{(k)}$ moving at velocity $\mathbf{V}^{(k)}$ in an otherwise quiescent fluid, and $\mathbf{r}^{(k)} \equiv \mathbf{x} - \mathbf{Y}^{(k)}$. Here, $\mathbf{Y}^{(k)}$ is the instantaneous location of the k th droplet. In Eq. (25), the combination $[\mathbf{V}^{(k)} - \mathbf{U}(\mathbf{Y}^{(k)}, t) - \mathbf{u}^{(k)}]$ represents the relative velocity between the k th droplet and the composite flow excluding the disturbance flow due to the k th droplet itself. Namely, $\mathbf{u}^{(k)}$ represents the disturbance flow velocity due to all droplets except the k th droplet, at the location of the k th droplet. Also, $\mathbf{u}^{(k)}$ is determined by applying the centerpoint approximation (Wang et al. 2005) to the boundary conditions $\tilde{\mathbf{U}}(|\mathbf{r}^{(k)}| = a^{(k)}, t) = \mathbf{V}^{(k)}$, yielding

$$\mathbf{u}^{(k)} = \sum_{\substack{m=1 \\ m \neq k}}^{N_p} \mathbf{u}_s[\mathbf{d}^{(mk)}; a^{(m)}, \mathbf{V}^{(m)} - \mathbf{U}(\mathbf{Y}^{(m)}, t) - \mathbf{u}^{(m)}], \quad (27)$$

for $k = 1, 2, \dots, N_p$,

where $\mathbf{d}^{(mk)} \equiv \mathbf{Y}^{(k)} - \mathbf{Y}^{(m)}$. The above equation represents a linear system of the dimension equal to $3N_p$. We note that $\mathbf{u}^{(k)}$ is a function of the background airflow field and the instantaneous locations and velocities of all droplets.

Since the Stokes flow induced by m th droplet decays with $\mathbf{d}^{(mk)}$ as $a^{(m)}/d^{(mk)}$, as an approximation, we may truncate the right hand side of Eq. (27) if $d^{(mk)}/a^{(m)} \geq C$, or only contributions from droplets in the neighbor-

hood are considered. The truncation radius C may be determined by a combined consideration of numerical accuracy and computational efficiency. The efficient cell index method with cell size equal to the truncation radius and the concept of linked lists (Allen and Tildesley 1987) were used here to quickly identify all the pairs participating in hydrodynamic interactions.

Results in this paper were based on $C = 50$. In Fig. 4, we show that the resulting collision efficiency is insensitive to the hydrodynamic interaction radius for $C > 20$. While the average velocity of the droplets does depend on C (Batchelor 1972), the relative motion relevant to collision interactions is not affected by the value of C if C is made larger than about 20. We note that, while the droplets are much smaller than the Kolmogorov scale, the hydrodynamic interaction radius is on the order of the Kolmogorov scale. Since the disturbance flows and hydrodynamic interactions were treated separately from the flow evolution, and since the dominant effect of hydrodynamic interactions is contributed by droplet pairs separated by a distance much less than the hydrodynamic interaction radius, our methodology is reasonable.

Once $\mathbf{u}^{(k)}$ is solved, the drag force acting on the k th droplet can be calculated simply as (Wang et al. 2005)

$$\mathbf{D}^{(k)} = -6\pi\mu a^{(k)}[\mathbf{V}^{(k)} - \mathbf{U}(\mathbf{Y}^{(k)}, t) - \mathbf{u}^{(k)}]. \quad (28)$$

The simulation typically involved 200 000 droplets, with half of the droplets of size 1, and second half of size 2. The simulation considered all hydrodynamic (i.e., 1–1, 1–2, 2–2) interactions, where 1–1 denotes hydrodynamic interactions among size-1 droplets, 1–2 denotes hydrodynamic interactions of size-1 droplets with size-2 droplets, and 2–2 hydrodynamic interactions among size-2 droplets.

c. Motion of droplets

Since the density of the droplet ρ_p is much larger than the air density ρ , the equation of motion for the k th droplet takes a relatively simple form (Maxey and Riley 1983)

$$\frac{dV_i^{(k)}(t)}{dt} = -\frac{V_i^{(k)}(t) - U_i[\mathbf{Y}^{(k)}(t), t] - u_i^{(k)}}{\tau_p^{(k)}} - g\delta_{i3}, \quad (29)$$

$$\frac{dY_i^{(k)}(t)}{dt} = V_i^{(k)}(t), \quad (30)$$

where $\tau_p^{(k)} = 2\rho_p(a^{(k)})^2/(9\rho\nu)$, g is the gravitational acceleration, and ν is the kinematic viscosity of air. In this study, we assume that $\rho_p = 1.0 \text{ g cm}^{-3}$, $\rho = 0.001 \text{ g cm}^{-3}$, and $\nu = 0.17 \text{ cm}^2 \text{ s}^{-1}$. The Stokes terminal velocity of k th droplet is $W^{(k)} = \tau_p^{(k)}g$. When only geometri-

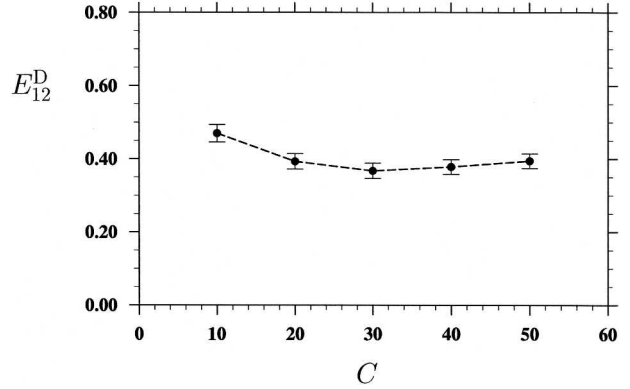


FIG. 4. Sensitivity of the computed dynamic collision efficiency with C .

cal collisions are considered, the hydrodynamic interaction velocities $u_i^{(k)}$ ($k = 1, 2, \dots, N_p$) are set to zero.

The droplets were introduced into the simulation when the background air turbulence had reached the statistically stationary stage. The initial conditions were that the locations of the droplets were randomly distributed and the initial velocity was set equal to the local fluid velocity plus the terminal velocity of the droplet. After about $3 \times \max(\tau_{p1}, \tau_{p2})$, data on collision-related statistics began to be accumulated to obtain running averages, to minimize any effect of the initial conditions. To closely simulate the number density in clouds, typically on the order of 100 000 size-1 droplets and 100 000 size-2 droplets were followed.

The turbulence field, disturbance flow velocities, and locations and velocities of all droplets were advanced in time simultaneously. For each time step, the following procedures were implemented:

- 1) Interpolate the undisturbed fluid velocities at the locations of the droplets, $\mathbf{U}(\mathbf{Y}^{(k)}, t)$, using six-point Lagrangian interpolation;
- 2) solve the disturbance velocities $\mathbf{u}^{(k)}$ using Eq. (27);
- 3) advance the velocities and locations of the droplets using Eqs. (29) and (30);
- 4) process collision detections or pair kinematic statistics; and
- 5) advance the undisturbed fluid turbulence field $\mathbf{U}(\mathbf{x}, t)$ using a pseudospectral method.

The computation of the disturbance velocities accounting for hydrodynamic interactions was the most time-consuming part of the simulations, taking about 70% to 80% of the CPU time. Methods to optimize the computation of the disturbance velocities were developed to speed up the code. The simulations were performed on National Center for Atmospheric Research's (NCAR) SGI Origin 3800 with 16 to 32 nodes

and OpenMP. For each parameter setting, a typical simulation with 4000 time steps (or more than 10 large-eddy turnover times), requires 5 to 10 h of real clock time.

d. Collision detections and computation of kinematic properties

The method for collision detection went through several iterations and the final version utilized the efficient cell index method and the concept of linked lists (Allen and Tildesley 1987). A collision detection grid was carefully chosen so that all collision events were counted and, at the same time, no time was wasted on processing pairs with large separations. While we were primarily interested in the 1–2 collision events, self-collisions (1–1 and 2–2) were also considered. A separate code was used to independently compute the kinematic properties $\langle |w_r(r)| \rangle$ and $g_{12}(r)$. For further details on collision detections and computation of kinematic properties, the readers are referred to Zhou et al. (1998) and Zhou et al. (2001).

4. Results and discussions

We shall first validate the correction factors under the same condition for which they were derived. In Fig. 5 we show the distributions of kinematic properties for a case of simple gravitational coagulation with the non-overlap requirement, before and after the corrections are applied. For this case, the expected kinematic values, when normalized, are equal to 1 as indicated by the thin horizontal lines in the figure. Therefore, the data before the corrections should overlap with the theoretical correction factors. This is indeed the case for all values of r within the limits of the numerical uncertainties, with corrections recovering the expected values. We note that the correction factor for g_{12} increases very quickly with r for $R \leq r \leq 2R$. The correction factor for the relative velocity has a minimum of 0.8301 at $r = 1.125R$, because of the strong effect of small radial velocity near the edge of the shaded region in Fig. 2 when r being close to R .

To further understand the effects of the nonoverlap condition, air turbulence, and hydrodynamic interactions, we report results from several case studies with and without air turbulence. We consider a system containing 50 000 droplets of radius $a_1 = 25 \mu\text{m}$ and 50 000 droplets of radius $a_2 = 20 \mu\text{m}$ in a 64^3 DNS simulations with $R_\lambda = 40$. For the six case studies (cases 1 through 6) shown in Tables 2 and 3, the simulation domain size was set to 8.329 cm; therefore, the number density for each size was about 86.5 cm^{-3} and the total liquid water

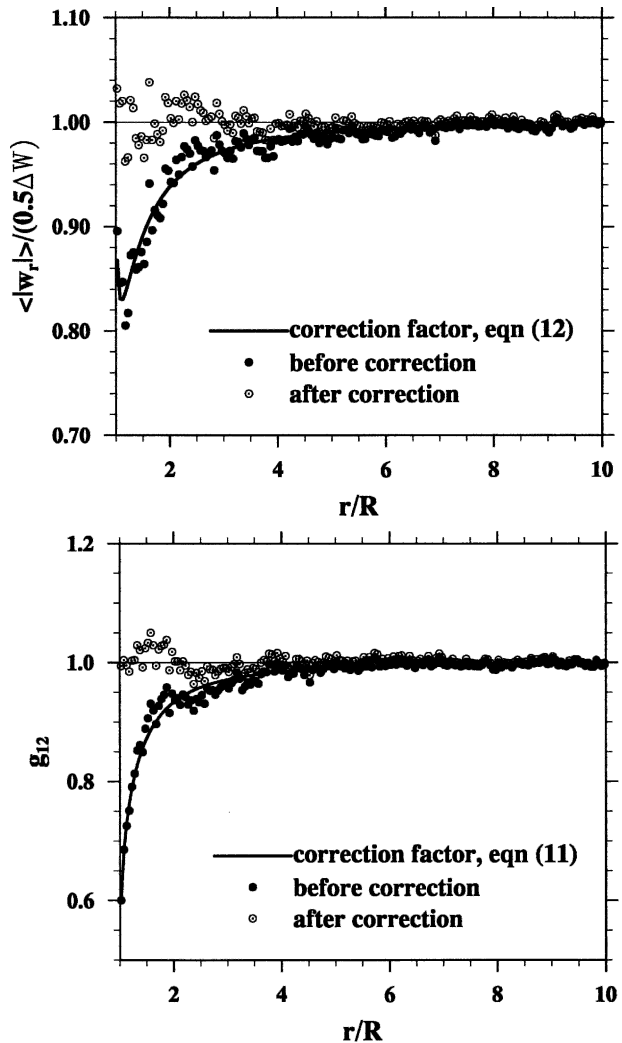


FIG. 5. Radial relative velocity and radial distribution function obtained with a shell thickness of $0.05R$, for gravitational coagulation with the nonoverlap requirement. Air turbulence was turned off and hydrodynamic interactions were not activated. The size-1 droplets have a radius of $25 \mu\text{m}$ and the size-2 droplets have a radius of $20 \mu\text{m}$.

content was 8.56 g m^{-3} . For the three case studies (cases 7 through 9) shown in Table 4, the simulation domain size was set to 11.80 cm, resulting in a number density of 30.43 cm^{-3} for each size and a total liquid water content of 3.01 g m^{-3} . The terminal velocity is 8.0147 cm s^{-1} for $25\text{-}\mu\text{m}$ droplets and 5.1294 cm s^{-1} for $20\text{-}\mu\text{m}$ droplets. The quantities used for normalization are $\Gamma_{12}^g = 1.836 \times 10^{-4} \text{ cm}^3 \text{ s}^{-1}$ and $W = 2.8853 \text{ cm s}^{-1}$. The time step size was set to $0.106\tau_{p2}$ for all runs, where τ_{p2} is the inertial response time of $20\text{-}\mu\text{m}$ droplets. Tests were made to ensure that the results do not change when the time step is further reduced.

To gain some understanding of the relative motion of

TABLE 2. A case study for geometric gravitational or hydrodynamic gravitational collisions.

	No HI, overlap (case 1)	No HI, nonoverlap (case 2)	HI (case 3)
$\Gamma_{12}^D/\Gamma_{12}^g$	1.006 ± 0.026	1.000 ± 0.026	0.257 ± 0.012
$\Gamma_{12}^K/\Gamma_{12}^g$ *	1.003 ± 0.035	1.026 ± 0.046	0.286 ± 0.023
	0.973 ± 0.079	1.007 ± 0.103	0.283 ± 0.051
$\langle w_r \rangle^{NO}/\Delta W^*$	—	0.447 ± 0.013	0.115 ± 0.005
	—	0.482 ± 0.028	0.157 ± 0.011
$\langle w_r \rangle^K/\Delta W^*$	0.499 ± 0.007	0.516 ± 0.013	0.132 ± 0.005
	0.496 ± 0.015	0.524 ± 0.030	0.147 ± 0.011
g_{12}^{NO} *	—	0.60 ± 0.02	0.653 ± 0.03
	—	0.53 ± 0.05	0.53 ± 0.06
g_{12}^K *	0.99 ± 0.02	0.99 ± 0.04	1.08 ± 0.04
	0.98 ± 0.05	0.97 ± 0.09	0.97 ± 0.10
$\Gamma_{11}^D/\Gamma_{12}^g$	—	—	0.00129 ± 0.00128
$\Gamma_{11}^K/\Gamma_{12}^g$ *	—	—	0.0121
	—	—	0.00513
$\Gamma_{22}^D/\Gamma_{12}^g$	—	—	0.00257 ± 0.00181
$\Gamma_{22}^K/\Gamma_{12}^g$	—	—	0.00281

* The first kinematic value was computed based on the shell $R \leq r < 1.05R$ and the second kinematic value on $R \leq r < 1.01R$.

colliding pairs, in Fig. 6 we show three trajectories of 20- μm droplets relative to 25- μm droplets for colliding pairs at three different levels of air turbulence, when hydrodynamic interactions were implemented (i.e., case 3, case 6, and case 9). For the case 3 run (Fig. 6a), the far-field relative motion is mostly along the vertical direction. However, even for this simplest case, droplets have finite velocity fluctuations because of the integral effect of the droplet–droplet hydrodynamic interactions (Batchelor 1972). This differs from the case of hydrodynamic–gravitational interaction of two isolated droplets. These velocity fluctuations induce some degree of spreading of the far-field relative motion so

(1), based on two isolated droplets, is not applicable to a suspension of droplets, even for the case of no air turbulence. The relative trajectories for the turbulent flow cases are much more complicated in three aspects: first, they are more curved and three-dimensional; second, the smaller droplets may approach from any direction relative to the larger droplets; and third, the relative velocity magnitude increases with the flow dissipation rate as indicated by the larger distance between two consecutive times shown in the relative trajectories. Therefore, air turbulence increases the relative velocity as well as the spreading in the angle of approach, both of which reflect the effect of the non-

TABLE 3. A case study for geometric turbulent or hydrodynamic turbulent collisions with $\epsilon = 400 \text{ cm}^2 \text{ s}^{-3}$.

	No HI, overlap (case 4)	No HI, nonoverlap (case 5)	HI (case 6)
$\Gamma_{12}^D/\Gamma_{12}^g$	1.446 ± 0.032	1.420 ± 0.032	0.584 ± 0.021
$\Gamma_{12}^K/\Gamma_{12}^g$ *	1.420 ± 0.056	1.544 ± 0.109	0.656 ± 0.052
	1.379 ± 0.113	1.585 ± 0.240	0.677 ± 0.111
$\langle w_r \rangle^{NO}/\Delta W^*$	—	0.486 ± 0.014	0.188 ± 0.006
	—	0.483 ± 0.032	0.184 ± 0.013
$\langle w_r \rangle^K/\Delta W^*$	0.565 ± 0.009	0.561 ± 0.015	0.218 ± 0.007
	0.540 ± 0.019	0.524 ± 0.034	0.201 ± 0.015
g_{12}^{NO} *	—	0.83 ± 0.03	0.91 ± 0.04
	—	0.83 ± 0.07	0.92 ± 0.08
g_{12}^K *	1.32 ± 0.03	1.38 ± 0.06	1.50 ± 0.07
	1.28 ± 0.06	1.52 ± 0.13	1.68 ± 0.15
$\Gamma_{11}^D/\Gamma_{12}^g$	0.542 ± 0.028	0.462 ± 0.025	0.415 ± 0.025
$\Gamma_{11}^K/\Gamma_{12}^g$ *	0.517	0.484	0.399
	0.504	0.475	0.408
$\Gamma_{22}^D/\Gamma_{12}^g$	0.121 ± 0.013	0.102 ± 0.012	0.0914 ± 0.0103
$\Gamma_{22}^K/\Gamma_{12}^g$ *	0.122	0.105	0.0961
	0.117	0.0851	0.0888

* The first kinematic value was computed based on the shell $R \leq r < 1.05R$ and the second kinematic value on $R \leq r < 1.01R$.

TABLE 4. A case study for geometric turbulent or hydrodynamic turbulent collisions with $\epsilon = 100 \text{ cm}^2 \text{ s}^{-3}$.

	No HI, overlap (case 7)	No HI, nonoverlap (case 8)	HI (case 9)
$\Gamma_{12}^D/\Gamma_{12}^g$	1.120 ± 0.032	1.117 ± 0.032	0.315 ± 0.016
$\Gamma_{12}^K/\Gamma_{12}^{g*}$	1.120 ± 0.073	1.180 ± 0.130	0.302 ± 0.048
	1.124 ± 0.150	1.311 ± 0.318	0.370 ± 0.129
$\langle w_r \rangle^{\text{NO}}/\Delta W^*$	—	0.463 ± 0.018	0.111 ± 0.010
		0.503 ± 0.041	0.142 ± 0.023
$\langle w_r \rangle^K/\Delta W^*$	0.515 ± 0.010	0.533 ± 0.020	0.129 ± 0.011
	0.496 ± 0.023	0.545 ± 0.044	0.154 ± 0.025
$g_{12}^{\text{NO}*}$	—	0.67 ± 0.04	0.71 ± 0.05
	—	0.66 ± 0.10	0.66 ± 0.11
$g_{12}^K^*$	1.09 ± 0.05	1.11 ± 0.08	1.17 ± 0.09
	1.14 ± 0.10	1.20 ± 0.18	1.20 ± 0.19
$\Gamma_{11}^D/\Gamma_{12}^g$	0.0491 ± 0.0098	0.0400 ± 0.0084	0.0412 ± 0.0089
$\Gamma_{11}^K/\Gamma_{12}^{g*}$	0.0465	0.0372	0.0482
	0.0466	0.0270	0.0148
$\Gamma_{22}^D/\Gamma_{12}^g$	0.0182 ± 0.0056	0.0164 ± 0.0053	0.0091 ± 0.0040
$\Gamma_{22}^K/\Gamma_{12}^{g*}$	0.0201	0.0211	0.0223
	0.0210	0.0152	0.0121

* The first kinematic value was computed based on the shell $R \leq r < 1.05R$ and the second kinematic value on $R \leq r < 1.01R$.

uniform, unsteady local airflow on the motion of droplets.

In Fig. 7, we display a few grazing trajectories of 20- μm droplets relative to 25- μm droplets for three different levels of air turbulence. Here, relative grazing trajectories were defined using pairs with minimum separation distance less than 1% collision radius but did not actually collide. While the relative motion is nearly vertical when there is no turbulence, the trajectories are strongly curved for the turbulent flow cases and as such pairs may approach from any relative directions in the far field, making the use of y_c inapplicable.

In Table 2, the air turbulence was turned off and three simulations are considered: the first case considers geometrical collisions with ghost droplets, the second case refers to geometrical collisions with nonoverlap droplets, and the third case the hydrodynamic-gravitational collisions. Care was taken to ensure that the total simulation time was less than $L_B/\Delta W$, so the periodic boundary condition is not affecting the results (e.g., Warshaw 1967). Here, L_B is the size of the computational domain and ΔW is the differential terminal velocity.

The first row in Table 2 shows that the dynamical collision kernels for 1–2 collisions are essentially the same for the first two cases and are equal to the theoretical value, while hydrodynamic interactions reduce the collision kernel to 25.7% of the geometrical kernel, or a collision efficiency of 0.257. This collision efficiency is the same as the collision efficiency obtained by finding the relative grazing trajectory based on two isolated droplets, that is, the result based on Eq. (1). This

serves as an excellent validation of our box-based simulations based on many droplets.

The uncertainty estimates shown in this table and others were computed based on observed variations in time, namely, by studying the variations of local-in-time spatial averages and assuming Gaussian statistics for the variations. In direct numerical simulations, a finite computational domain (typically on the order of 10 cm) containing a finite number of droplets is used; therefore, collision counts and other average values at a given instant do not represent the expected values over a much larger volume. Since the system is assumed to be stationary and homogeneous, the expected values can be approached by averaging further over time. The variations from one time to another, therefore, provides a natural means to estimate the uncertainties of our results.

The second row in Table 2 gives the kinematic collision kernel after the nonoverlap corrections have been taken (which is needed for case 2 and case 3). The numerical uncertainties here are larger than those for the dynamical collision kernel, because the droplet sizes and volume fraction are very small, leading to a very small chance of finding two droplets almost in touch or a small sample of pairs available for computing the kinematic properties. However, within the numerical uncertainties, we can claim that the kinematic collision kernel is the same as the dynamic collision kernel for all the three cases in Table 2. The kinematic values before the nonoverlap corrections are shown as row 3 and row 5 while the kinematic values after corrections are shown as row 4 and row 6; it is shown how the

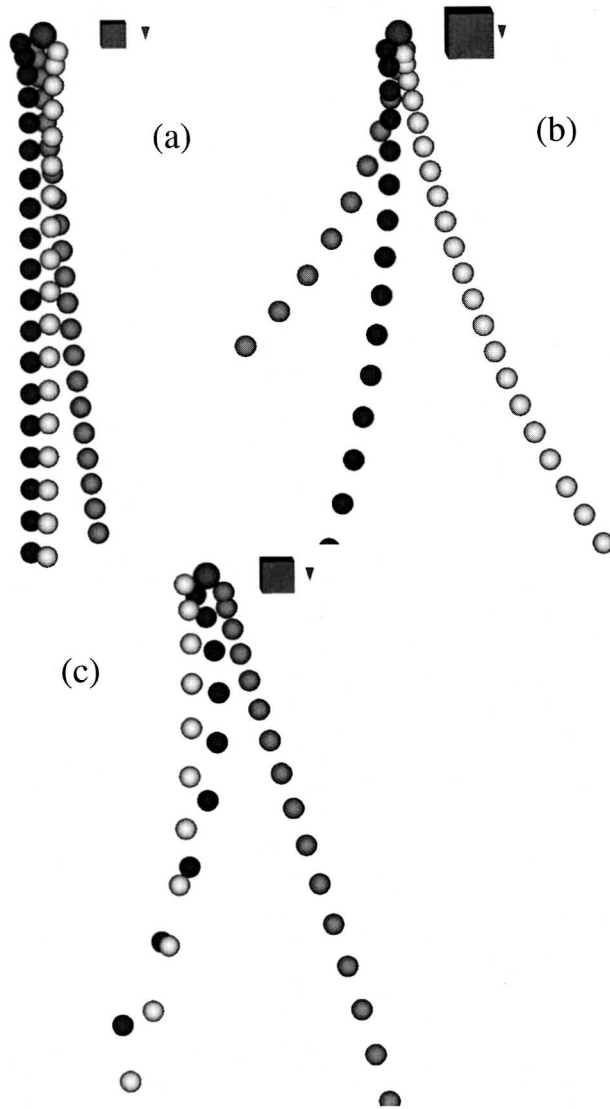


FIG. 6. The trajectories of 20- μm droplets seen by 25- μm droplets for three colliding droplet pairs with hydrodynamic interactions: (a) suspension without turbulence; (b) turbulent suspension at $\epsilon = 100 \text{ cm}^2 \text{ s}^{-3}$; (c) turbulent suspension at $\epsilon = 400 \text{ cm}^2 \text{ s}^{-3}$. The time interval was set to 0.0022 s or about 42% the inertial response time of the 20- μm droplet. The interval is 4 times the actual time step size used. The small cube in (a) has an edge length equal to collision radius, while the small cube in (b) and (c) has an edge length equal to 10% flow Kolmogorov length. The small cone next to the cube indicates the direction of gravity.

expected values are restored by the nonoverlap corrections. The corrected kinematic properties (row 4 and row 6 in Table 2) reveal that the main effect of hydrodynamic interactions is to reduce the relative radial velocities for the 1–2 pairs. There is also some evidence here (also see Fig. 10 below) that the hydrodynamic interactions result in a slight accumulation of pairs even without fluid turbulence. Both these effects are illus-

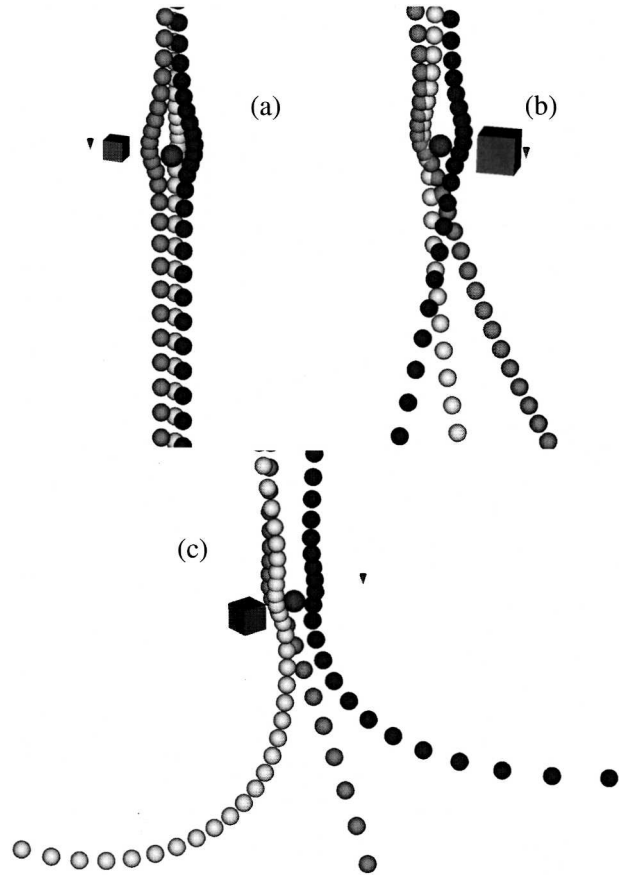


FIG. 7. Three grazing trajectories of 20- μm droplets relative to 25- μm droplets with hydrodynamic interactions: (a) suspension without turbulence; (b) turbulent suspension at $\epsilon = 100 \text{ cm}^2 \text{ s}^{-3}$; (c) turbulent suspension at $\epsilon = 400 \text{ cm}^2 \text{ s}^{-3}$. The time interval was set to 0.0022 s or about 42% the inertial response time of the 20- μm droplet.

trated in Fig. 8 qualitatively. When droplets of size 2 approach a droplet of size 1, their relative velocities change in both direction and magnitude, leading to significantly reduction in the radial relative velocities. Some level of nonuniform pair concentration can also be caused by the changing relative motion shown in the illustration.

During the course of the simulation for case 3, we also detected one 1–1 collision and two 2–2 collisions. These self-collisions are not possible without hydrodynamic interactions. However, hydrodynamic interactions result in velocity fluctuations, leading to nonzero relative motion even for equal-size droplets. Of course, the level of velocity fluctuations and relative motion increases with the droplet volume concentrations. For cloud applications, the concentrations are so low, the magnitude of self-collision kernels without turbulence is two to three orders of magnitude smaller than the 1–2

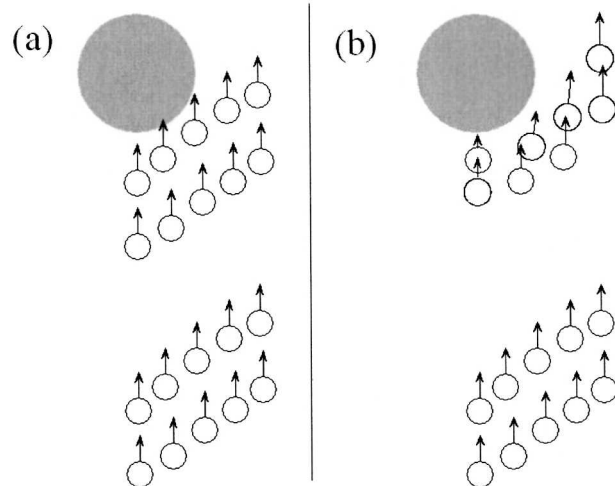


FIG. 8. Sketch to illustrate the effects of hydrodynamic interactions on the relative radial velocities and distribution of droplet-droplet pairs (a) without and (b) with hydrodynamic interactions.

collision kernel, so this is not important. However, self-collisions could become more important if the volume concentrations are higher. Kinematic formulations based on extension of gravitational coagulation such as Eq. (19) will not be able to describe self-collision kernels, but our general formulation can handle this situation.

The cases shown in Table 3 are similar to the cases in Table 2, but now the background air turbulence is switched on with an average dissipation rate of $400 \text{ cm}^2 \text{ s}^{-3}$. The Kolmogorov scales are $\eta = 591 \text{ } \mu\text{m}$, $\tau_k = 0.0206 \text{ s}$, and $v_k = 2.87 \text{ cm s}^{-1}$. The Stokes numbers for the two droplet sizes are 0.396 and 0.254, while the nondimensional terminal velocities W/v_k are 2.791 and 1.786. Therefore, the differential terminal velocity is $\Delta W = 1.005v_k$. Turbulence enhances the geometrical collision kernel by over 40%, as shown in row 1 of Table 3. The true collision efficiency for turbulent flow is $E_{12} \approx 0.584/[(1.420 + 1.446)/2] = 0.408$, therefore, turbulence also increases the collision efficiency by a factor of $0.408/0.257 = 1.59$. The net increase in collision kernel due to turbulence is by a factor of 2.28. The levels of enhancement by turbulence depend on the flow dissipation rate and flow Reynolds number.

Once again, within the numerical uncertainties, the kinematical collision kernel is the same as the dynamical collision kernel for all the three cases (cases 4 through 6) when the shell thickness is equal to 1% R . For a shell thickness of 5% R , the kinematic collision kernel is slightly larger because both kinematic properties increase with r near $r = R$, see Fig. 9. This shows that the correction factors work well for the turbulent

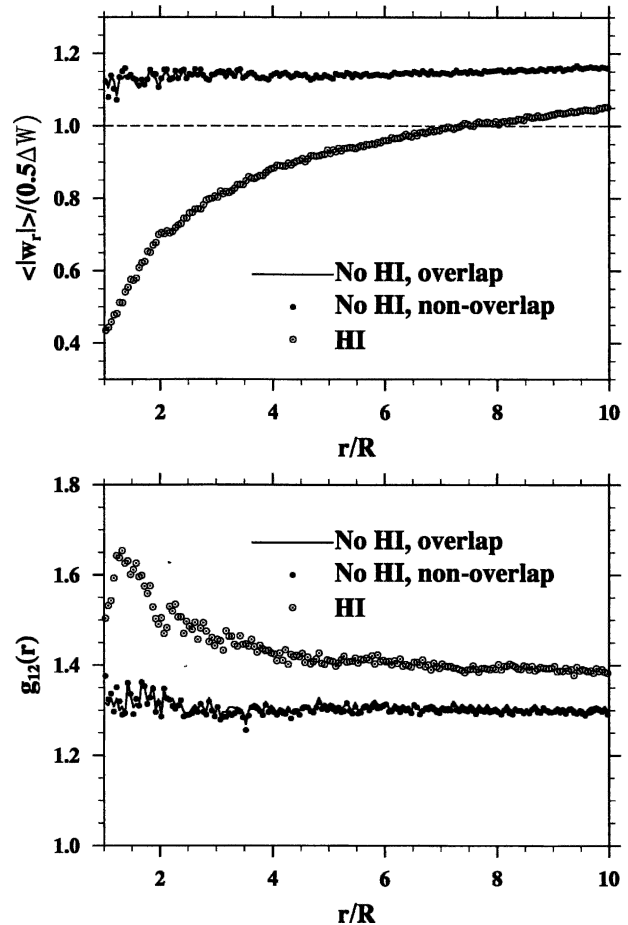


FIG. 9. Radial relative velocity and radial distribution function for 1-2 turbulent coagulation for cases 4 through 6. Note that the solid lines overlap with the solid circles in both plots and could only be identified for small r/R . The dash line indicates the value of 1 in both plots.

cases. We note that the kinematic results depend on the shell thickness in the sense that both $\langle |w_r| \rangle$ and g_{12} depend on r even near $r = R$, so the use of a thick shell may not reproduce the correct kinematic kernel since only near-contact pairs are relevant for the true kinematic kernel. On the other hand, the numerical uncertainties are larger with smaller shell thickness due to the smaller number of pairs possible. The comparison with the dynamic collision kernels should take both aspects into consideration.

The kinematic properties show that, for the case of turbulent flow, the hydrodynamic interactions reduce the radial relative velocity by a factor of 0.387, but increase the radial distribution function by a factor of 1.11. In the absence of turbulence, the hydrodynamic interactions reduce the radial relative velocity by a factor of 0.260, but increase the radial distribution function by a factor of 1.09. Therefore, hydrodynamic interac-

tions become less effective in changing the radial relative motion when droplets are suspended in a turbulent flow—this is the main reason for the increase in collision efficiency by turbulence.

This decreasing influence of hydrodynamic interactions on relative motion may be understood as follows. First, in a turbulent flow, the droplet–droplet relative velocity is larger in magnitude, so hydrodynamic interactions could not act as effectively because of the finite inertia of droplets and the larger relative velocity. Second, the orientation of relative motion also has a random character and could change because of the local turbulent velocity field; this may also weaken the effect of hydrodynamic interactions, which tend only to reorient the relative motion away from the pair radial direction. Similar qualitative arguments have been proposed in Pinsky et al. (1999).

Finally, the 1–1 self-collision kernel (0.415) with hydrodynamic interactions is now comparable to the 1–2 collision kernel (0.584), even the geometric 1–1 self-collision kernel $[(0.542 + 0.462)/2 = 0.502]$ is only about 1/3 of the geometric 1–2 collision kernel (1.433). In other words, the 1–1 self-collision efficiency is much higher than the 1–2 collision efficiency. This could have important implications to the broadening of droplet size spectrum. Similar observation can also be made regarding the 2–2 self-collision efficiency.

The relative importance of the turbulence effect changes with the flow dissipation rate. In Table 4, results are shown for the same droplet sizes as in Table 3 but with a flow dissipation rate at $100 \text{ cm}^2 \text{ s}^{-3}$. Now the Kolmogorov scales are: $\eta = 837 \text{ }\mu\text{m}$, $\tau_k = 0.0412 \text{ s}$, and $v_k = 2.03 \text{ cm s}^{-1}$. The Stokes numbers for the two droplet sizes are 0.198 and 0.127, while the nondimensional terminal velocities W/v_k are 3.947 and 2.526. Therefore, the differential terminal velocity is $\Delta W = 1.421v_k$. The true collision efficiency for the turbulent flow is $E_{12} = 0.315/[(1.120 + 1.117)/2] = 0.282$, so at this level of flow dissipation, turbulence increases the collision efficiency by a factor of $0.282/0.257 \approx 1.10$ only. The enhancement factor on the geometrical collision rate is about 1.12. The overall enhancement by turbulence is about a factor of 1.23, which is much smaller than 2.28 for the case of $\epsilon = 400 \text{ cm}^2 \text{ s}^{-3}$. The 1–1 self-collision kernels are at least one order of magnitude smaller than for the case of $\epsilon = 400 \text{ cm}^2 \text{ s}^{-3}$. Since the effective concentrations are also smaller, the numerical uncertainties in Table 4 are larger than those shown in Table 3.

In Fig. 10 we display the radial relative velocity and radial distribution function for 1–2 pairs for the same cases discussed in Table 2. The relative velocities for the first two cases without HI are the same and do not depend on r , as expected. With HI, the relative velocity

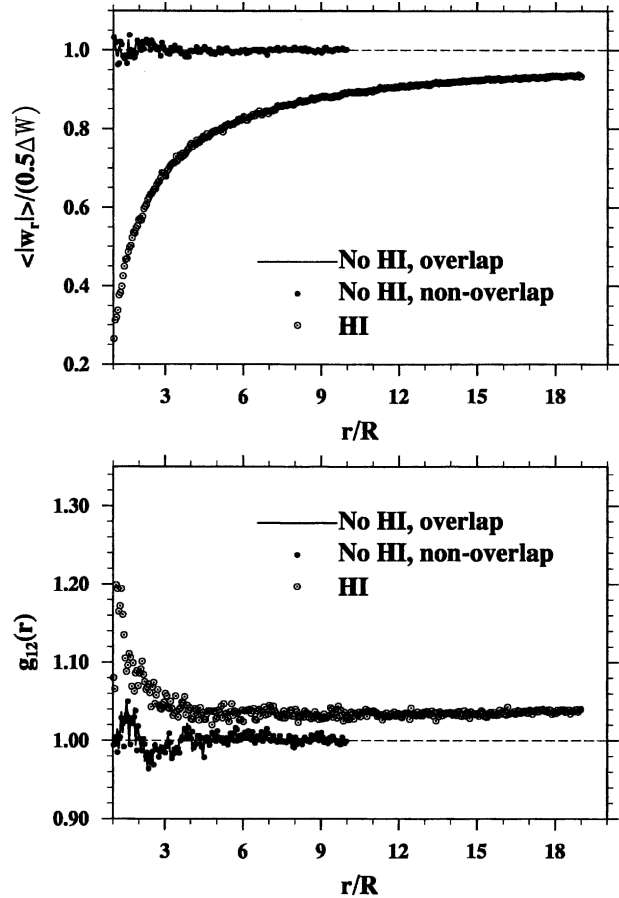


FIG. 10. Radial relative velocity and radial distribution function for 1–2 gravitational coagulation cases. Note that the solid lines overlap with the solid circles in both plots and could only be identified for small r/R . The dash lines indicate the value of 1 in both plots.

decreases sharply as r/R approaches 1, indicating that the effect of HI is mostly effective at short separation distances. It is interesting to note that, on the other hand, the relative velocity is still affected by HI for r/R as large as 20. In fact, there is no reason to expect that the relative motion and the pair distribution for hydrodynamically interacting droplets would approach the results of no hydrodynamic interaction, as the separation distance increases. The reason is that the motion of each droplet has already been modified by the presence of all other droplets in the system. It needs to be stressed that we consider hydrodynamic interactions among all droplets, not just hydrodynamic interactions between two given droplets. In statistical mechanics, the fact that finite-range, many-body interactions change two-particle statistics over all separations is well known. Similarly, the radial distribution functions for the first two cases without HI are the same and do not

depend on r . For the case with HI, the radial distribution function is significantly larger than one for short separation distances, for the reason as illustrated in Fig. 8. Interestingly, the peak values occurs when $1.125 \leq r/R \leq 1.325$. This can be explained by the curved path of the grazing trajectory. The actual inaccessible region due to nonoverlap is slightly larger than what is shown in Fig. 2. Therefore, the correction factor for g_{12} at contact would be even less than what is given by Eq. (11), or the corrected value of g_{12} should be slightly larger than what is shown in Fig. 10. The curved path of the grazing trajectory implies that a refined theory for g_{12} and $\langle |w_r| \rangle$ at contact may be desirable. There is a finite difference in g_{12} between the HI case and no HI cases for large r , being about 0.041 at $r/R = 10$.

In Fig. 9, we show the radial relative velocity and radial distribution function for 1–2 pairs for the same cases discussed in Table 3. Again, the results for the first two cases are the same and show little dependence on r . The reduction in the relative velocity because of hydrodynamic interactions is less steep as r approaches R , when compared to the still air case as shown in Fig. 10. The peak location for g_{12} can be more clearly identified at $r/R = 1.325$. Also the relative increase in g_{12} because of HI is now about 0.092 for $r/R = 10$, more than twice the value for the still air case. This is a combining effect of far-field preferential accumulation and near-field HI augmentation.

Finally, we show the kinematic properties for 1–1 turbulent self-collisions in Fig. 11 for $\epsilon = 400 \text{ cm}^2 \text{ s}^{-3}$. Since there is no differential terminal velocity for equal-size droplets, the relative velocity is mainly created by the local flow shear and is linearly related to r (Saffman and Turner 1956). This relative motion is roughly $0.03v_k$ (or about $0.03\Delta W$) at contact. This is much weaker than the relative motion between the two droplet sizes. As a result, the effect of HI on self-collisions is much smaller as the force due to disturbance flows is almost negligible. The value of g_{11} is significantly larger than one for short separations due to the preferential concentration effect; HI has very little effect on the value of g_{11} . For the HI case, g_{11} displays a peak at $r/R = 1.275$. This implies a large collision efficiency for 1–1 self collisions.

5. Conclusions and remarks

A methodology for conducting three-dimensional, time-dependent, direct numerical simulations of hydrodynamically interacting droplets in the context of cloud microphysics has been developed. This allows us to address droplet–fluid turbulence interactions and droplet–droplet interactions in a more consistent simulation

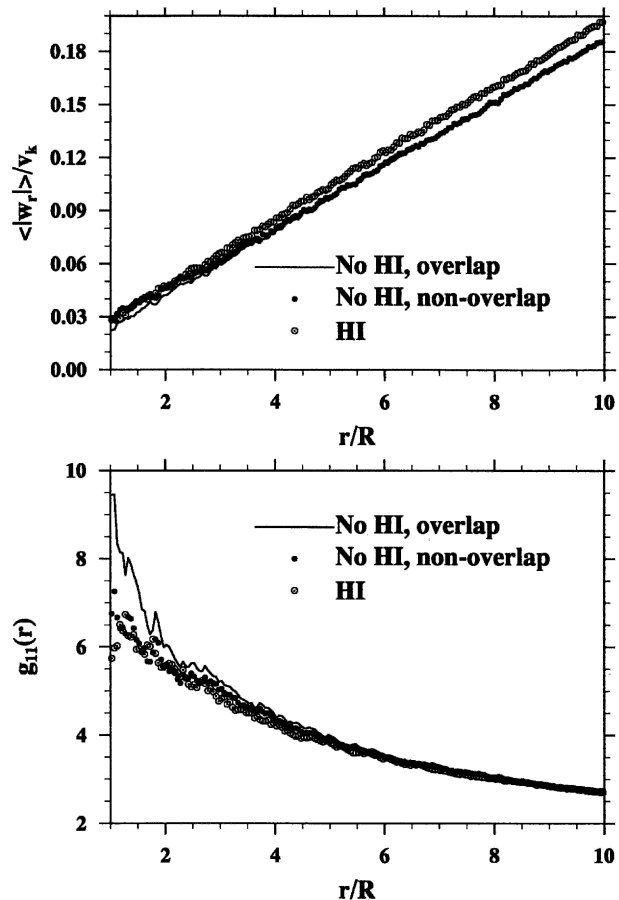


FIG. 11. Radial relative velocity and radial distribution function for 1–1 turbulent self collisions for cases 4 through 6.

framework than what had been known previously. This represents a significant step forward in view of previous lack of quantitative research tools in this area. The range of length scales covered in each direction is from about $10 \mu\text{m}$ (the droplet size) to about 10 cm (the computational domain size), roughly four orders of magnitude. As with other computational methods, only a finite range of length scales can be covered, and we chose to cover the smallest end of length scales in cloud microphysics, as it is assumed that physics at this end has the dominant impact on the collision rates of droplets. The larger scales uncovered in our simulations could also play a significant role. For example, the much higher flow Reynolds numbers in real clouds imply a much stronger intermittency of vortical structures at the Kolmogorov scale. Large-scale, spatially nonuniform fluid accelerations could also have a secondary effect on the collision rate if the droplets were brought into collisions by different larger-scale fluid eddies. At this stage, it is not clear how these effects can be handled. Using best computing resources to increase

the range of length scales (or flow Reynolds number) in the simulations only provides a limited, partial solution. Therefore, on the one hand, the simulation methodology provides crucial insights and quantitative information needed to accurately model the effects of turbulence on collision rate and collision efficiency. On the other hand, unknown formulation-related uncertainties, other than the numerical uncertainties discussed in the paper, must always be kept in mind when interpreting our results.

A critical literature review indicates that theoretical formulation capable of handling particle–particle collisions under hydrodynamic interactions in a turbulent flow is lacking. In this work, we have developed and validated a kinematic formulation capable of quantitatively addressing the collision kernel for such a general situation. Although formally this formulation is the same as the formulation recently developed to describe geometrical collision rate of finite-inertia, nonsettling particles (Sundaram and Collins 1997; Wang et al. 1998b, 2000), its application to hydrodynamically interacting droplets requires corrections because of the non-overlap requirement. We have proposed the correction rules and have validated these against DNS results. Our formulation is more general than previously published formulations in this journal (de Almeida 1976; Grover and Pruppacher 1985; Koziol and Leighton 1996; Pinsky et al. 1999) that, in most cases, are some extension of the description of gravitational collision.

A general kinematic representation of the collision efficiency, consistent with the true dynamic collision efficiency, has been introduced. This has led to the observation that hydrodynamic interactions have a decreasing influence on the relative radial velocity in a turbulent flow, when compared to the pure hydrodynamic gravitational problem. This is the main reason that turbulence enhances the collision efficiency, in addition to augmenting the geometric collision rate. We also observe that hydrodynamic interactions increase the nonuniformity of near-field pair density distribution, resulting in higher radial distribution function at contact when compared to the geometric collision case. Our formulation separates the effect of turbulence on collision efficiency from the previously observed effect of turbulence on the geometric collision rate.

The level of increase in collision efficiency by turbulence appears to be larger than the results of Koziol and Leighton (1996), but smaller than the values obtained by Pinsky et al. (1999). A preliminary comparison with the studies of Koziol and Leighton (1996) and Pinsky et al. (1999) is shown in Fig. 12 for $a_1 = 20 \mu\text{m}$ and $\epsilon = 100 \text{ cm}^2 \text{ s}^{-3}$. Uncertainties of our results are indicated. We note that the results for the base case without turbu-

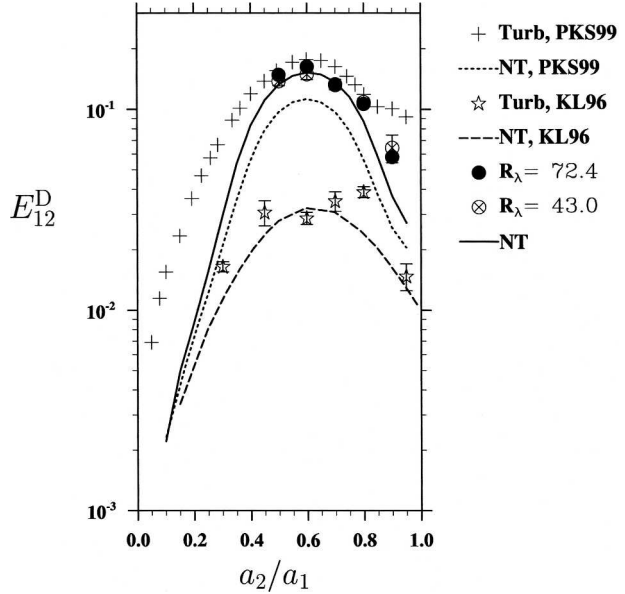


FIG. 12. Comparison of preliminary results of collision efficiencies with previous published results for $a_1 = 20 \mu\text{m}$. Here, KL96 is Koziol and Leighton (1996) and PKS99 represents Pinsky et al. (1999). The flow dissipation rate ϵ was set to $100 \text{ cm}^2 \text{ s}^{-3}$ in all studies. In the legend, NT stands for the results without air turbulence and Turb for results with air turbulence.

lence are different. With exact Stokes flow representation in which the lubrication force is correctly represented, Koziol and Leighton (1996) obtained a much smaller collision efficiency for the base case. However, as discussed in Wang et al. (2005), the exact Stokes flow representation with no-slip boundary conditions tends to underestimate the collision efficiency because of the slip effect at very small separations. On the other hand, Pinsky et al. (1999) gives the largest collision efficiency for the base case because the superposition method they used is not accurate. With the improved superposition method (Wang et al. 2005), our results for the base case are believed to be more realistic. Unlike the work of Koziol and Leighton (1996), where the turbulence cannot be seen to have a definite effect on the collision efficiency, our results does show a definite effect for droplets of similar sizes, a qualitative trend also shown in Pinsky et al. (1999). The relative enhancement because of turbulence from our results, however, is smaller than that of Pinsky et al. (1999).

There is also evidence that the collision efficiency for collisions among equal-size droplets is much higher than that for collisions between unequal droplets. The link between collision efficiency and the relative velocity implies that the effect of turbulence on collision efficiency may even be greater for real clouds as R_λ is much higher in reality than the value of R_λ realized in

this work. The enhancement factors due to air turbulence discussed in this paper may be viewed as lower bounds of those in reality.

Acknowledgments. This study has been supported by the National Science Foundation through Grant ATM-0114100 and by the National Center for Atmospheric Research. NCAR is sponsored by the National Science Foundation. Most of the simulations were conducted using the SGI Origin 3800/2100 at NCAR. OA is grateful to the additional computing resources provided by the Scientific Computing Division at NCAR.

REFERENCES

- Allen, M. P., and D. J. Tildesley, 1987: *Computer Simulation of Liquids*. Oxford University Press, 385 pp.
- Arenberg, D., 1939: Turbulence as a major factor in the growth of cloud droplets. *Bull. Amer. Meteor. Soc.*, **20**, 444–445.
- Batchelor, G. K., 1972: Sedimentation in a dilute dispersion of spheres. *J. Fluid Mech.*, **52**, 245–268.
- Beard, K. V., and H. T. Ochs, 1993: Warm-rain initiation: An overview of microphysical mechanisms. *J. Appl. Meteor.*, **32**, 608–625.
- Davis, M. H., and J. D. Sartor, 1967: Theoretical collision efficiencies for small cloud droplets in Stokes flow. *Nature*, **215**, 1371–1372.
- de Almeida, F. C., 1976: The collisional problem of cloud droplets moving in a turbulent environment—Part I: A method of solution. *J. Atmos. Sci.*, **33**, 1571–1578.
- , 1979: The collisional problem of cloud droplets moving in a turbulent environment. Part II: Turbulent collision efficiencies. *J. Atmos. Sci.*, **36**, 1564–1576.
- Dodin, Z., and T. Elperin, 2002: On the collision rate of particles in turbulent flow with gravity. *Phys. Fluids*, **14**, 2921–2924.
- Franklin, C. N., P. A. Vaillancourt, M. K. Yau, P. Bartello, 2005: Collision rates of cloud droplets in turbulent flow. *J. Atmos. Sci.*, **62**, 2451–2466.
- Grabowski, W. W., and P. Vaillancourt, 1999: Comments on “Preferential concentration of cloud droplets by turbulence: Effects on the early evolution of cumulus cloud droplet spectra.” *J. Atmos. Sci.*, **56**, 1433–1436.
- Grover, S. N., and H. R. Pruppacher, 1985: The effect of vertical turbulent fluctuations in the atmosphere on the collection of aerosol-particles by cloud drops. *J. Atmos. Sci.*, **42**, 2305–2318.
- Jonas, P. R., 1996: Turbulence and cloud microphysics. *Atmos. Res.*, **40**, 283–306.
- Klett, J. D., and M. H. Davis, 1973: Theoretical collision efficiencies of cloud droplets at small Reynolds numbers. *J. Atmos. Sci.*, **30**, 107–117.
- Koziol, A. S., and H. G. Leighton, 1996: The effect of turbulence on the collision rates of small cloud drops. *J. Atmos. Sci.*, **53**, 1910–1920.
- Maxey, M. R., 1987: The gravitational settling of aerosol-particles in homogeneous turbulence and random flow fields. *J. Fluid Mech.*, **174**, 441–465.
- , and J. J. Riley, 1983: Equation of motion for a small rigid sphere in a nonuniform flow. *Phys. Fluids*, **26**, 883–889.
- Pinsky, M., A. Khain, and M. Shapiro, 1999: Collisions of small drops in a turbulent flow. Part I: Collision efficiency. Problem formulation and preliminary results. *J. Atmos. Sci.*, **56**, 2585–2600.
- Pruppacher, H. R., and J. D. Klett, 1997: *Microphysics of Clouds and Precipitation*. 2d ed. Kluwer Academic, 954 pp.
- Reade, W. C., and L. R. Collins, 2000: Effect of preferential concentration on turbulent collision rates. *Phys. Fluids*, **12**, 2530–2540.
- Saffman, P. G., and J. S. Turner, 1956: On the collision of drops in turbulent clouds. *J. Fluid Mech.*, **1**, 16–30.
- Shaw, R. A., 2003: Particle–turbulence interactions in atmospheric clouds. *Annu. Rev. Fluid Mech.*, **35**, 183–227.
- Squires, K. D., and J. K. Eaton, 1990: Particle response and turbulence modification in isotropic turbulence. *Phys. Fluids*, **A2**, 1191–1203.
- Sundaram, S., and L. R. Collins, 1997: Collision statistics in an isotropic, particle-laden turbulent suspension. *J. Fluid Mech.*, **335**, 75–109.
- Vaillancourt, P., and M. Yau, 2000: Review of particle–turbulence interactions and consequences for cloud physics. *Bull. Amer. Meteor. Soc.*, **81**, 285–298.
- Wang, L.-P., and M. R. Maxey, 1993: Settling velocity and concentration distribution of heavy particles in homogeneous isotropic turbulence. *J. Fluid Mech.*, **256**, 27–68.
- , A. S. Wexler, and Y. Zhou, 1998a: On the collision rate of small particles in isotropic turbulence. Part 1. Zero-inertia case. *Phys. Fluids*, **10**, 266–276.
- , —, and —, 1998b: Statistical mechanical descriptions of turbulent coagulation. *Phys. Fluids*, **10**, 2647–2651.
- , —, and —, 2000: Statistical mechanical descriptions of turbulent coagulation of inertial particles. *J. Fluid Mech.*, **415**, 117–153.
- , O. Ayala, and W. W. Grabowski, 2005: Improved formulations of the superposition method. *J. Atmos. Sci.*, **62**, 1255–1266.
- Warshaw, M., 1967: Cloud droplet coalescence: Statistical foundations and a one-dimensional sedimentation model. *J. Atmos. Sci.*, **24**, 278–286.
- Zhou, Y., A. S. Wexler, and L.-P. Wang, 1998: On the collision rate of small particles in isotropic turbulence. Part 2. Finite-inertia case. *Phys. Fluids*, **10**, 1206–1216.
- , —, and —, 2001: Modelling turbulent collision of bidisperse inertial particles. *J. Fluid Mech.*, **433**, 77–104.